A first-principles predictive model of the pedestal height and width: development, testing and ITER optimization with the EPED model

IOP Publishing and International Atomic Energy Agency Nuclear Fusion
Nucl. Fusion **51** (2011) 103016 (8pp) doi:10.1088/0029-5515/51/10/103016

A first-principles predictive model of the pedestal height and width: development, testing and ITER optimization with the EPED model

P.B. Snyder[1], R.J. Groebner[1], J.W. Hughes[2], T.H. Osborne[1], M. Beurskens[3], A.W. Leonard[1], H.R. Wilson[4] and X.Q. Xu[5]

[1] General Atomics, PO Box 85608, San Diego, CA 92186-5608, USA
[2] MIT Plasma Science and Fusion Center, Cambridge, MA, USA
[3] EURATOM/UKAEA Fusion Association, Culham Science Centre, Abingdon, UK
[4] York Plasma Institute, Department of Physics, University of York, Heslington,York YO10 5DD, UK
[5] Lawrence Livermore National Laboratory, Livermore CA, USA

E-mail: snyder@fusion.gat.com

Received 1 February 2011, accepted for publication 25 July 2011
Published 19 August 2011
Online at stacks.iop.org/NF/51/103016

Abstract
We develop and test a model, EPED1.6, for the H-mode pedestal height and width based upon two fundamental and calculable constraints: (1) onset of non-local peeling–ballooning modes at low to intermediate mode number, (2) onset of nearly local kinetic ballooning modes at high mode number. Calculation of these two constraints allows a unique, predictive determination of both pedestal height and width. The present version of the model is first principles, in that no parameters are fit to observations, and includes important non-ideal effects. Extensive successful comparisons with existing experiments on multiple tokamaks, including experiments where predictions were made prior to the experiment, are presented, and predictions for ITER are discussed.

(Some figures in this article are in colour only in the electronic version)

1. Introduction

The pressure at the top of the edge transport barrier (or 'pedestal height') in tokamaks strongly impacts global confinement and fusion performance. Accurately predicting the pedestal height in ITER and demonstration power plants is an essential element of prediction, and a powerful tool for optimization, of fusion performance.

The spontaneous formation of the edge barrier (or 'L-Mode to H-Mode transition') creates a near-step (or 'pedestal') in the pressure profile across the radially outermost few per cent of the confined plasma (figure 1(*a*)). Pedestal formation both increases the global pressure and broadens the pressure profile, in part because of the physics of gradient-scale-length driven core turbulence, resulting in a dramatic improvement of both global confinement and global stability, with both generally increasing with the height of the pedestal.

Inside the edge barrier itself, the dynamics are complex and quite different than in the core plasma. Turbulence levels are typically much reduced from L-mode edge values. $E \times B$ shearing rates are high, and generally increase as the pedestal height increases, due to the increase in the ion diamagnetic term, which is proportional to the ion pressure gradient. In what we refer to here as 'high-performance' H-modes, the pedestal generally continues to rise until strong limiting instabilities are triggered, which constrain the growth of the pedestal and can determine its structure (though other mechanisms, including remnant turbulence and neoclassical transport, can be important in understanding the detailed dynamics). In this paper, we develop and test a predictive model (EPED) for the pedestal structure based on two key limiting instabilities, non-local peeling–ballooning (P–B) modes, and nearly local kinetic ballooning modes (KBMs). Combining these two constraints allows prediction of two unknowns, the pedestal height and width. These predictions can be made prior to experiments on existing devices, and can also be used to predict and optimize performance of future devices such as ITER. The present version of the model (EPED1.6) has no parameters fit to observations, and its predictions are determined entirely from P–B and KBM theory using the computational methods described below.

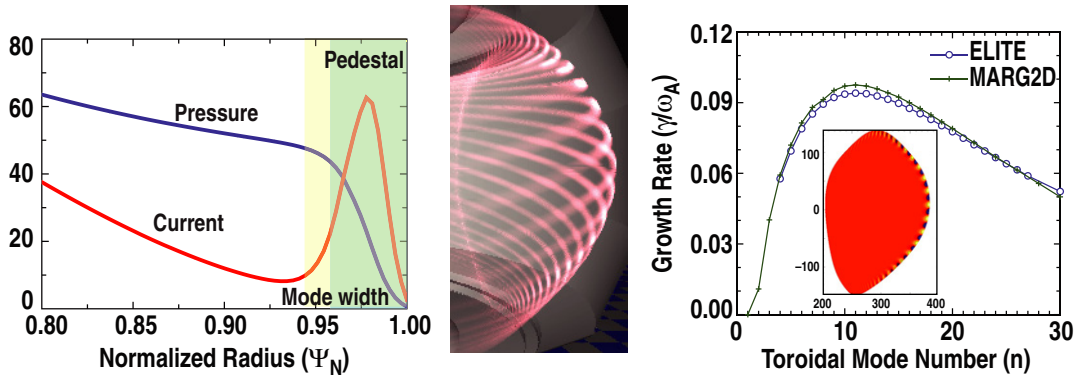

Figure 1. (*a*) Illustration of typical H-mode pressure and current profiles with the edge barrier or 'pedestal' region dark shaded, and the P–B mode width (light shaded), extending across and beyond the pedestal. (*b*) Calculated 3D structure of an $n = 18$ P–B mode in the DIII-D tokamak. (*c*) Benchmark of P–B growth rates between the ELITE and MARG2D codes for a realistic equilibrium truncated at the 99.8% flux surface. The $n = 11$ 2D mode structure is the inset (blue and yellow contours on orange background).

The physics of the P–B mode is briefly reviewed in section 1.1, along with the method for calculating the P–B constraint in the EPED1.6 model. In section 2, the KBM is described, along with the new 'ballooning critical pedestal' (BCP) technique used to calculate this constraint in the EPED1.6 model. Section 3 describes the complete EPED1.6 model, as well as discussing how it can be simplified to yield the previous EPED1 model. Section 4 presents a series of tests of EPED1.6 on existing devices, and section 5 presents EPED1.6 predictions and initial optimization for ITER.

1.1. The P–B mode constraint

The strong pressure gradient, and resulting large bootstrap current, in the edge barrier region (figure 1(*a*)) provide free energy to drive intermediate wavelength MHD instabilities, which are known as 'peeling–ballooning' (P–B) modes, due to the coupling of the pressure-gradient driven ballooning and current-driven peeling/kink drives. While early studies of P–B coupling employed the local, high toroidal mode number (high-n) limit [1], it is important to emphasize that these modes are fundamentally non-local in character, with significant finite-n effects, and a radial extent that is typically comparable to, or wider than, the edge barrier [2–8], as shown in figure 1(*a*). A typical 3D structure of an $n = 18$ P–B mode is shown in figure 1(*b*).

The P–B stability boundary is evaluated by calculating mode growth rates across a broad range of toroidal mode numbers (typically $n \sim 3 - 30$), with an efficient MHD code, such as ELITE [2, 3, 9], which has been developed and optimized specifically for this purpose. ELITE has been extensively and successfully tested against other MHD stability codes [2, 3, 5, 9]. An example, showing a successful benchmark of the ELITE and MARG2D [10, 11] codes is given in figure 1(*c*).

Investigation of P–B stability has led to improved understanding of important constraints on the pedestal height and the mechanism for edge-localized modes (ELMs). The combination of high-resolution pedestal diagnostics, including substantial recent improvements, and highly efficient stability codes, has made edge stability analysis more routine on several major tokamaks, contributing both to understanding and to experimental planning and performance optimization. Extensive testing has led to substantial confidence in the accuracy of the calculated P–B constraint on the pedestal height (e.g. [2, 4–8]). A recent compilation of results on several devices [5] notes that observed maximum pedestal height and ELM onset condition agree with the calculated P–B constraint within measurement uncertainty across a substantial sample size.

The tests of the P–B model described above generally rely on equilibria reconstructed after experiments, incorporating profiles measured with high-resolution diagnostics, and perturbing around measured profiles to construct stability diagrams. To invoke P–B stability predictively, we have developed a technique using model equilibria characterized by a small set of scalar parameters [4, 5]. These model equilibria are designed to have simple functional forms for the profiles, while capturing the characteristics important for P–B stability (particularly plasma shape, pedestal profiles and bootstrap current) sufficiently to allow quantitatively accurate calculations of stability bounds. Example model equilibrium profiles for an ITER baseline study are given in figure 2. P–B stability studies using model equilibria successfully account for observed trends in pedestal height with plasma shape, collisionality, magnetic field (B_T) and current (I_p) [4, 5]. In those calculations, the width of the pedestal is an input. The P–B stability calculation itself provides a constraint on the pedestal height as a function of the width. This relation is rather complex in general due to the non-locality of the P–B modes; that is, it is not a simple gradient limit. However, the relationship can be readily calculated as shown in figure 3 for a pair of DIII-D discharges described in [12, 13], and generally, the P–B constraint on the pedestal height is found to scale roughly with the 3/4 power of the pedestal width ($\beta_{Nped} \sim \Delta_{\psi_N}^{3/4}$, where β_{Nped} is the Troyon normalized pedestal pressure and Δ_{ψ_N} is the width of the pedestal in normalized poloidal flux, as defined by a fit to a tanh in [4]). Hence, as the pedestal width increases, the maximum stable pedestal height increases less than linearly, and the maximum stable gradient decreases.

In the EPED1.6 model, the ELITE code is used to evaluate MHD growth rates for $n = (5, 6, 8, 10, 15, 20, 30)$. A growth rate threshold is determined by a model of

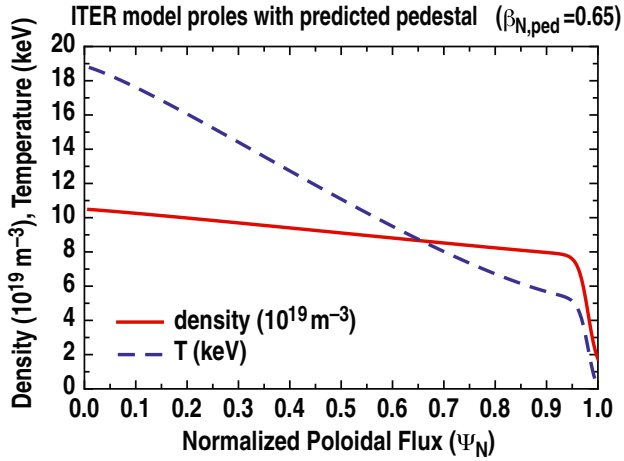

Figure 2. Temperature and density profile shapes used in the model equilibria, with tanh-shaped edge barriers. Profiles shown are for an ITER model equilibrium with $\beta_{\mathrm{Nped}} = 0.65$.

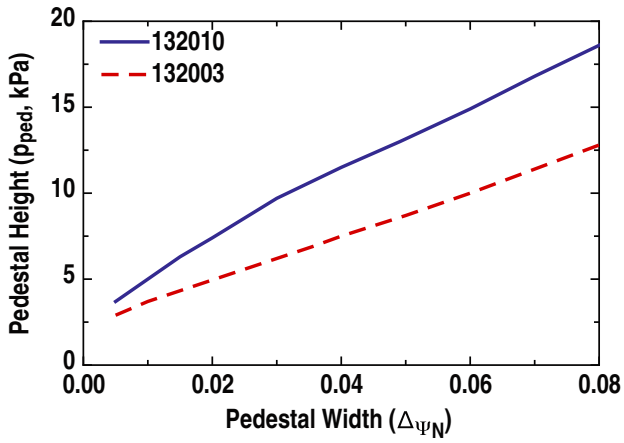

Figure 3. Calculated P–B stability boundary as a function of pedestal width (Δ_{ψ_N}) for input parameters based on two DIII-D discharges (132003 and 132010), using the model equilibrium technique. Note that the P–B stability boundary increases sub-linearly with pedestal width.

diamagnetic stabilization. The simple analytic relation $-\gamma^2_{\mathrm{MHD}} = \omega(\omega - \omega_*)$ [14, 15] predicts that the ideal MHD growth rate, γ_{MHD} must be larger than half the ion diamagnetic frequency (ω_*) for instability. However, the analytic theory is derived in the limit of constant ω_*, while in the edge barrier, ω_* has a strong radial variation. This variation can be approximately taken into account by defining an effective diamagnetic frequency, $\omega_{*\mathrm{eff}}$, such that $-\gamma^2_{\mathrm{MHD}} = \omega(\omega - \omega_{*\mathrm{eff}})$, and the threshold for instability is $\gamma_{\mathrm{MHD}} > \omega_{*\mathrm{eff}}/2$. We employ the results of a two-fluid stability calculation using the BOUT++ code [16, 17]. This calculation self-consistently takes into account the rapid variation of the diamagnetic frequency across the edge barrier. Calculating both the ideal growth rate (γ_{MHD}) and the 2-fluid growth rate, $\gamma_{2F} = Im(\omega)$, determines the effective diamagnetic frequency $\omega_{*\mathrm{eff}} = 2\sqrt{\gamma^2_{\mathrm{MHD}} - \gamma^2_{2\mathrm{F}}}$ for a range of toroidal mode numbers n. The resulting values of $\omega_{*\mathrm{eff}}$ are shown as filled circles in figure 4, normalized to the Alfvén frequency, $\omega_{\mathrm{A}} = v_{\mathrm{A}}/R$, where v_{A} is the Alfvén speed and R is the geometric major

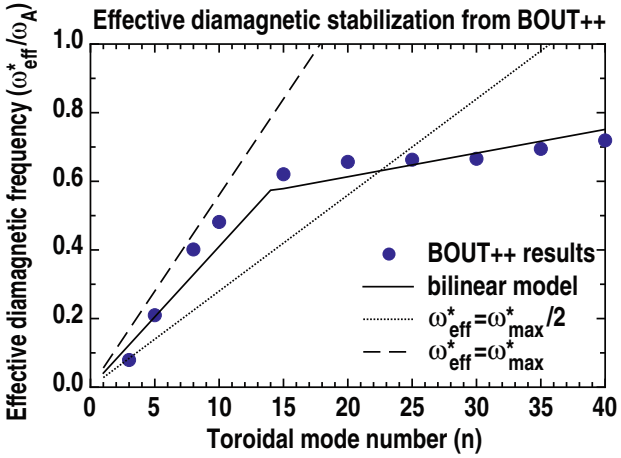

Figure 4. Effective diamagnetic stabilization coefficient, $\omega_{*\mathrm{eff}}$, evaluated via a non-local calculation using the BOUT++ code (filled circles), in units of the Alfvén frequency. A bilinear model fit to the BOUT++ results is also shown (solid line), and is employed in the EPED1.6 model. For comparison, the values of the half maximum diamagnetic frequency (dotted line, used in prior EPED1 model) and the maximum diamagnetic frequency (dashed line) in the edge barrier are also shown.

radius. A simple bilinear fit to this calculation (solid line in figure 4) is employed in the EPED1.6 model. The transition point in the bilinear fit is defined to occur at a critical value of n, such that $n_{\mathrm{crit}} q_{95} = 27.7$, where q_{95} is the safety factor at the 95% flux surface. Note that the previous version of the EPED model, EPED1, used a value of $\omega_{*\mathrm{eff}}$ fixed to the half maximum value of ω_* in the edge barrier (for the case shown in figure 4, this value is shown with a dotted line). Compared with this previous version, the updated diamagnetic stabilization model in EPED1.6 provides somewhat stronger stabilization at low n and significantly weaker stabilization at higher n. The use of this updated model is particularly important in smaller tokamaks where ω_*/v_{A} tends to be relatively large, especially for studies of high collisionality plasmas where higher n modes tend to limiting, as frequently is the case in the Alcator C-Mod tokamak.

The effects of toroidal flow on P–B mode stability have been studied, for example with ELITE [9] and MINERVA [11]. While sheared flow is typically destabilizing at long wavelengths and stabilizing at short wavelengths, the effect on the overall P–B stability boundary is generally small (a few per cent or less) [9, 11]. Hence for simplicity and efficiency, the effects of toroidal flow are not included in the P–B calculation in the EPED model.

The P–B constraint on the pedestal height can then be determined as a function of the width as described above, including a model of diamagnetic stabilization. However, a second constraint is required in order to predict both the pedestal height and width. That second constraint is provided by KBM onset, as described in the following section.

2. The KBM constraint

The EPED series of models employ local onset of the KBM, as a second constraint. For EPED1.6, a simplified form of the KBM constraint is developed using a 'BCP' technique, in

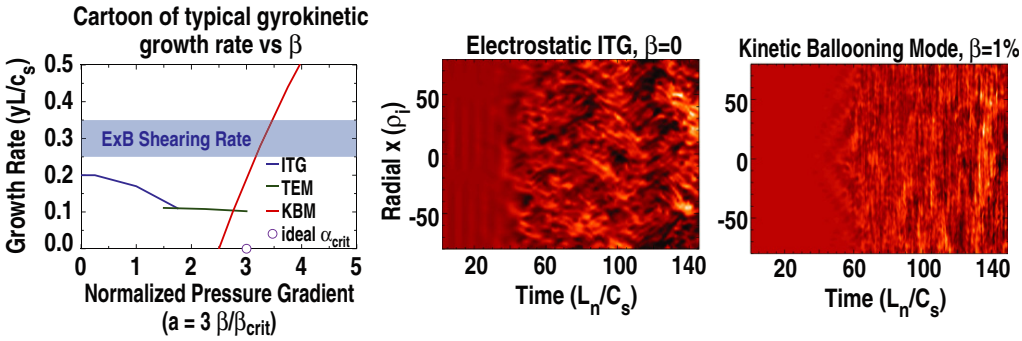

Figure 5. (*a*) Schematic diagram of gyrokinetic growth rates for the ITG, TEM and KBM as a function of normalized pressure gradient. The KBM attains a large growth rate, exceeding typical $E \times B$ shearing rates, in the vicinity of the local ballooning critical gradient (open circle). (*b*) Time evolution of ITG and (*c*) KBM turbulence from electromagnetic gyrofluid simulation [20, 21]. The KBM exhibits short correlation times and high transport levels.

which an edge barrier profile is taken to be ballooning critical when the central half of it is at or beyond the local ballooning threshold.

The KBM has been extensively studied in linear and nonlinear gyrofluid and gyrokinetic simulations, as well as semi-analytic treatments (e.g. [18–23]). The KBM can be considered as the kinetic analogue of the local MHD ballooning mode, and has a similar threshold for instability in the limit of zero ion temperature gradient, and a somewhat lower threshold, due to ion drift resonance, at finite ion temperature gradient [18–21]. A schematic diagram of KBM stability is shown in figure 5(*a*). As the plasma pressure gradient is increased (at fixed density and temperature scale length), the ion temperature gradient mode is stabilized somewhat by finite-β effects, and eventually, near the MHD ballooning limit, the KBM is destabilized. The KBM onset is highly stiff, in that the growth rate becomes large at pressure gradients only marginally above the threshold. Both quasi-linear estimates and nonlinear simulations find that KBM-driven transport rises to large levels near threshold [18–23]. An example contrasting electrostatic ITG turbulence with electromagnetic KBM turbulence is shown in figures 5(*b*) and (*c*). While ITG and KBM turbulence have similar spatial scales, KBM turbulence is characterized by short correlation times and very large heat and particle transport (heat and particle diffusion coefficients normalized to gyro-Bohm $\gg$1) [20, 21].

To develop a simple, numerically efficient model of the KBM constraint, we make the approximations that KBM onset is highly stiff (transport will balance sources at a gradient near the onset value), and that the onset condition can be approximated as the MHD local ballooning limit. The first approximation is well justified by simulation results, and the second is found to be surprisingly accurate (within $\sim$10%) in standard aspect ratio tokamaks, due to the partial offset of destabilizing (ion drift resonance) and stabilizing (FLR, $E \times B$ shear stabilization) effects. As shown in figure 5(*a*), the KBM growth rate rises to large values, where $E \times B$ shear stabilization is overcome, and large transport fluxes are driven, in the vicinity of the local MHD ballooning limit (open circle).

Criticality to the KBM provides an approximately local constraint, which we wish to integrate across the edge barrier to generate a relationship between the pedestal height and width. In principle, this integration can be performed by constructing profiles, which are ballooning critical at all radial points in the edge barrier. However, in practice, with realistic equilibria with self-consistent bootstrap current and fixed total current, this becomes a highly complex, non-local problem. A more efficient approach is to choose a simple functional form for the profiles in the edge barrier, and then increase the pedestal height at each fixed width until the profile is at or beyond criticality across half of the edge barrier (and thus, on average, approximately critical across the whole barrier). The 'BCP' approach employs the same sets of model equilibria previously used for P–B stability studies (figures 2 and 6(*a*) and [4, 5]), which have tanh-shaped density and temperature profiles in the edge barrier, and self-consistent bootstrap current calculated with the Sauter model. At each value of the pedestal width, the pedestal height is increased until the profile is at or beyond criticality across the central half of the profiles, as shown in figure 6(*a*). This defines a relationship between the pedestal height and width at criticality that can be calculated as a function of the model equilibrium input parameters. The BCP technique is reasonably robust, but it does require that the profile reach criticality locally as the pedestal pressure is increased, and that the region that is at or beyond (i.e. deeply unstable or 2nd stable) criticality is well defined and bounded. This requirement is generally met for standard aspect ratio plasmas at weak to moderate shaping, but can break down for very strong shaping and/or low aspect ratio. A future update to the model involving gyrokinetic calculations is planned to address these cases. Exploration of non-local effects on the KBM is an important direction for future work.

Calculations of the KBM constraint using the BCP technique are shown in figures 6(*b*) and (*c*). For each value of the pedestal width ($\Delta_{\psi_N} = 0.03, 0.04, \ldots, 0.08$), the pedestal height is increased until the BCP criterion is met. The filled symbols show calculations, and dashed and dotted lines show parametric fits to those calculations. Figure 6(*b*) shows the calculation for model equilibrium parameters typical of a DIII-D and an expected ITER discharge. Despite substantial differences in these parameters (e.g. minor radius of 0.6 m versus 2 m, major radius of 1.66 m versus 6.2 m, B_t of 2 T versus 5.3 T, I_p of 1.2 MA versus 12 MA) and associated dimensionless parameters, the KBM constraint in terms of poloidal beta at the pedestal top ($\beta_{p,ped}$) is very similar in the two cases, approximately $\Delta_{\psi_N} = 0.089\beta_{p,ped}^{1/2}$, as shown by the

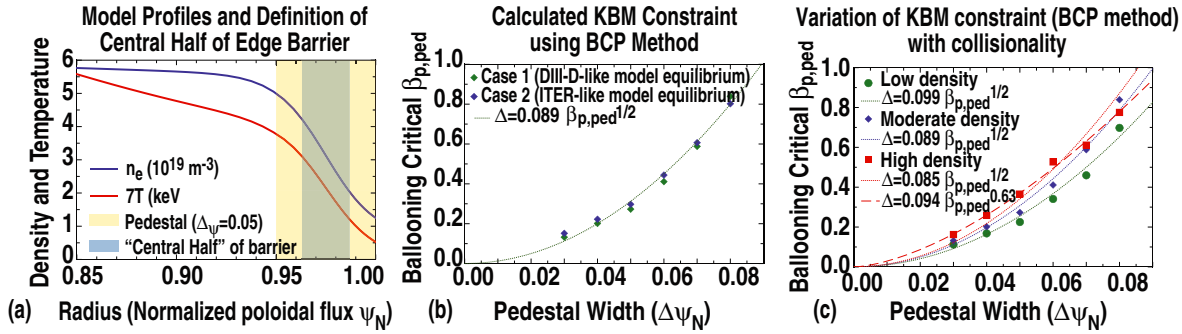

Figure 6. (*a*) Edge profiles for a model equilibrium illustrate the pedestal region (light shaded) and the central half (dark shaded) of the barrier which must be at or beyond criticality in the BCP technique. (*b*) The KBM constraint, calculated with the BCP technique, for two different model equilibria (DIII-D-like and ITER-like) shows a dominant $\beta_{p,ped} \sim \Delta_{\psi_N}^2$, or equivalently, $\Delta_{\psi_N} \sim \beta_{p,ped}^{1/2}$, dependence (dotted line). (*c*) The calculated KBM constraint shows a relatively weak but complex dependence on density (i.e. collisionality).

dotted line in figure 6(*b*). Note that this approximate $\Delta_{\psi_N} \propto \beta_{p,ped}^{1/2}$ dependence is expected, due to the characteristics of ballooning stability in the bootstrap-current dominated regime of the edge barrier in standard aspect ratio shaped tokamaks [12]. Generally, the BCP calculated KBM constraint can be written in the form of $\Delta_{\psi_N} = \beta_{p,ped}^{1/2} G(\nu_*, \varepsilon, \ldots)$ where G is a weakly varying function of collisionality (ν_*), aspect ratio (ε) and other dimensionless parameters, with values typically in the range 0.07–0.1 for standard aspect ratio shaped tokamaks.

3. The EPED pedestal model

The P–B and KBM constraints described in the previous two sections can then be combined to yield a predictive model (EPED1.6) for the pedestal height and width. The inputs ($\boldsymbol{I}$) to the model are eight scalar parameters which are used to define the model equilibria, $I = [B_t(\mathrm{T}), I_p(\mathrm{MA}), R(\mathrm{m}), a(\mathrm{m}), \delta, \kappa, n_{e,ped}(10^{19}\,\mathrm{m}^{-3}), \beta_{N,global}]$, where R is the geometric major radius, a is the minor radius, δ is the triangularity, κ is the elongation, $n_{e,ped}$ is the pedestal electron density and $\beta_{N,global}$ is the global Troyon normalized β. The first six input parameters, describing plasma shape and fields, are generally well known for future devices as well as future experiments on existing devices. The accuracy to which the final two parameters, which determine pedestal collisionality and global Shafranov shift, are known varies depending on the device and control methods employed. When necessary, EPED predictions can be made over a range in these parameters. The outputs of the EPED model are the pedestal height, usually given as a pressure (p_{ped}) or a normalized pedestal beta ($\beta_{N,ped}$), and the pedestal width in normalized poloidal flux (Δ_{ψ_N}). Note that in comparisons with experiment, the measured width is defined to be the average of the electron temperature and density widths as discussed in [12], and that the model predicts only this average, not any separate variation of the temperature and density widths.

An illustration of the EPED1.6 model is given in figure 7. The solid line shows the calculated P–B constraint, the dotted line is the KBM constraint, and the solid diamond shows their intersection, the EPED1.6 predicted pedestal height and width. As discussed in section 1, the EPED model supposes that confinement in the edge barrier is so good that profiles will continue to rise until strong limiting instabilities, the P–B and

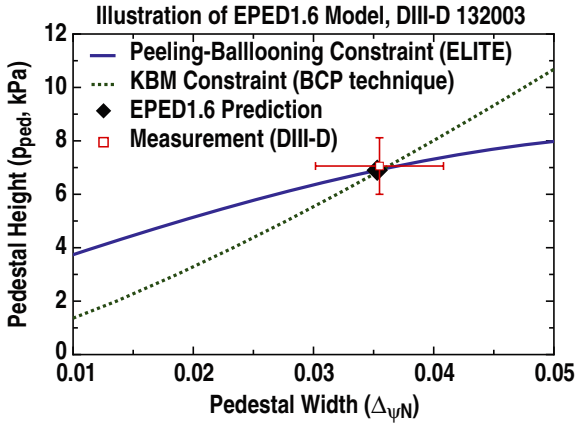

Figure 7. The EPED1.6 model predicts a pedestal height and width (solid diamond) from the intersection of calculated P–B (solid line) and KBM (dotted line) constraints. This can then be compared with observations, here shown by an open square, for DIII-D discharge 132003.

KBM, are triggered. Hence, following the transition into high-performance H-mode, the initially narrow and stable (below both lines and to the left of the diamond in figure 7) barrier will steepen until the KBM boundary is reached locally, and then follow the KBM critical contour (dotted line) up and to the right until the P–B boundary is reached, at the point marked by the diamond. The edge barrier will then hover near (Quiescent H-Mode or small ELM regimes) or execute a limit cycle around (large ELM regimes) this point in parameter space, and in either case, the diamond provides a reasonable approximation to the expected pedestal height and width in quasi-steady high-performance H-mode.

Note that the differing functional dependences of the P–B ($p_{ped} \sim \Delta_{\psi_N}^{3/4}$) and KBM ($p_{ped} \sim \Delta_{\psi_N}^2$) constraints ensure a unique nontrivial solution, and that the predicted height and width both depend on both the P–B and KBM constraints. That is, if either constraint is systematically incorrect, both the predicted height and width will be systematically incorrect, and hence both aspects of the model can be tested against measurements of the pedestal height (which is relatively easy to measure) as well as the width. Note also that the pedestal height can be maximized either by *improving* P–B stability (raising solid line in figure 7), or, counter-intuitively, by *degrading*

KBM stability (lowering dotted line). For the case shown in figure 7, EPED1.6 predictions were made for a DIII-D experiment described in [12, 13], and the measured pedestal height and width for DIII-D shot 132003 are shown by the open symbol, with error bars indicating an estimated 15% measurement uncertainty. In this case, the model is in good agreement with both the measured pedestal height and width.

3.1. The EPED1 model

A simple version of the EPED model, EPED1 [12], emphasizes the dominant dependence of the KBM constraint on $\beta_{\mathrm{p,ped}}$. Here we show how EPED1 can be obtained via simplification of the techniques used to derive EPED1.6. As noted above, for standard aspect ratio shaped tokamaks, the BCP calculated KBM constraint takes the form $\Delta_{\psi_{\mathrm{N}}} = \beta_{\mathrm{p,ped}}^{1/2} G(\nu_*, \varepsilon, \ldots)$ where G is a weakly varying function. This constraint can be approximated by taking an ensemble average over relevant sets of input parameters $\boldsymbol{I}$. Using the BCP technique, and 16 sets of input parameters (four each typical of DIII-D, JET, AUG and ITER), we find an ensemble average $\langle G \rangle = 0.084 \pm 0.010$. For historical reasons [12], the value $\langle G \rangle = 0.076$ is used in EPED1, leading to the simplified KBM constraint $\Delta_{\psi_{\mathrm{N,EPED1}}} = 0.076 \beta_{\mathrm{p,ped}}^{1/2}$.

The P–B constraint in EPED1 is directly calculated using ELITE on model equilibria specified by the input parameters $\boldsymbol{I}$ as described in section 1.1. A simple model of diamagnetic stabilization is employed via a growth rate threshold $\gamma_{\mathrm{MHD}} > \omega_{*\mathrm{pi}}/2$, where $\omega_{*\mathrm{pi}}$ is the half maximum value of the ion diamagnetic frequency in the edge barrier (illustrated by the dotted line in figure 4). The simplicity and efficiency of the EPED1 model have allowed it to be tested against large sets of data, including multiple experiments in which predictions were made before the experiment was conducted.

3.2. The EPED1.6 model

In the current version of the model, EPED1.6, both the P–B and KBM constraints are directly calculated for each set of inputs $\boldsymbol{I}$, leading to a model that is first principles in the sense that all aspects are derived and no reference is made to observations.

Beyond the dominant $\Delta_{\psi_{\mathrm{N}}} \propto \beta_{\mathrm{p,ped}}^{1/2}$ dependence of the KBM constraint, additional dependences, such as that on collisionality (ν_*), can be explored using the BCP technique. An example is shown in figure 6(*c*), in which the reference pedestal density (blue diamonds) is increased by 50% (red squares) or decreased by 25% (green circles). As shown by the fits to each case, both the coefficient, and at high ν_*, the exponent of the KBM constraint vary somewhat with ν_*. The variation with ν_* is complex, depending on shape and other parameters, so a parametrization is not straightforward. Hence, in EPED1.6, the KBM constraint is calculated directly for each case with the BCP technique, allowing the secondary dependences to be accurately accounted for (at the cost of additional complexity and computation). For each set of inputs, the BCP technique is employed at $\Delta_{\psi_{\mathrm{N}}} = 0.03$, 0.04, 0.05, 0.07, and a curve fit specific to each $\boldsymbol{I}$ is used to generate the KBM constraint.

The P–B constraint is calculated with ELITE as above, with the addition of a more sophisticated diamagnetic stabilization model which accounts for the rollover in diamagnetic stabilization at high-n. This model is developed via a fit to self-consistent calculations of diamagnetic stabilization of P–B modes using the BOUT++ code [16, 17], as described in section 1.1.

4. Experimental tests of the EPED1.6 model

The EPED model has been extensively tested across a range of experiments on several devices. The prior EPED1 model has been the subject of several experimental tests. For example, a dedicated experiment to test the model was conducted on DIII-D, in which EPED1 predictions were made before the experiment, and plasma current, toroidal field and triangularity were varied by a factor of 3, to yield more than an order of magnitude variation in the pedestal height, and a factor of 3 variation in the pedestal width. The EPED1 model was found to be in good agreement with the observations, with a ratio of predicted to observed pedestal height of 1.03 ± 0.13, and of width of 0.93 ± 0.15 in 17 discharges [12, 13]. Comparisons of the EPED1 model with pedestal height measurements on JT-60U [5, 24], JET [5, 25–27] and AUG [27] have found similar levels of agreement, generally within ~20%. The EPED1 model has recently been automated, allowing comparisons with large datasets, whose results will be reported in the near future.

The new EPED1.6 model is tested against the observed pedestal height in a set of 7 DIII-D and 7 JET discharges. The DIII-D discharges used in the comparison are 131996, 131997, 131999, 132003, 132006, 132007 and 131498, which are taken from an experiment in which plasma current and magnetic field were scanned to strongly vary pedestal conditions [12, 13], and from an ITER demonstration experiment [28]. The seven JET discharges studied are from a set of experiments designed to study pedestal variation as a function of normalized gyroradius [25–27, 29]. Together, these 14 cases encompass a large range of variation in pedestal height (1.6–22 kPa), normalized gyroradius ρ^*_{ped} (0.24–0.7), ν^* (0.3–5), and β_{ped} (0.3–1.2%), with a ratio of predicted to observed pedestal height of 1.02 ± 0.21, as shown in figure 8(*a*) (and on a log scale in (figure 8(*b*))). The EPED1.6 model is also consistent with the weak or zero dependence of pedestal width on gyroradius observed on JET and DIII-D [13, 26, 27, 29].

The compact, high field Alcator C-Mod tokamak [30] provides an excellent platform to test the EPED model in a parameter regime well separated from that on DIII-D or JET. It also allows tests of the model in H-mode plasmas heated predominantly by ion cyclotron resonance frequency (ICRF) heating. The relatively high collisionality and diamagnetic frequency on C-Mod are expected to strenuously test the improved diamagnetic stabilization model and collision-dependent KBM model specific to EPED1.6.

A new set of C-Mod experiments has been designed to test the model in an ICRF-heated H-mode regime with ELMs, with variation in the plasma current from ~686 kA to ~935 kA. This set of experiments is conducted in a low elongation shape ($\kappa \sim 1.45$), which has been found to be conducive to steady operation with ELMs on Alcator C-Mod [31]. A set of six discharges is studied, with $a \sim 21.7$ cm, $R \sim 67.5$ cm, $\delta \sim 0.47$, $B_{\mathrm{t}} \sim 5.4$ T and $\beta_{\mathrm{N,global}} \sim 1.1$. The low

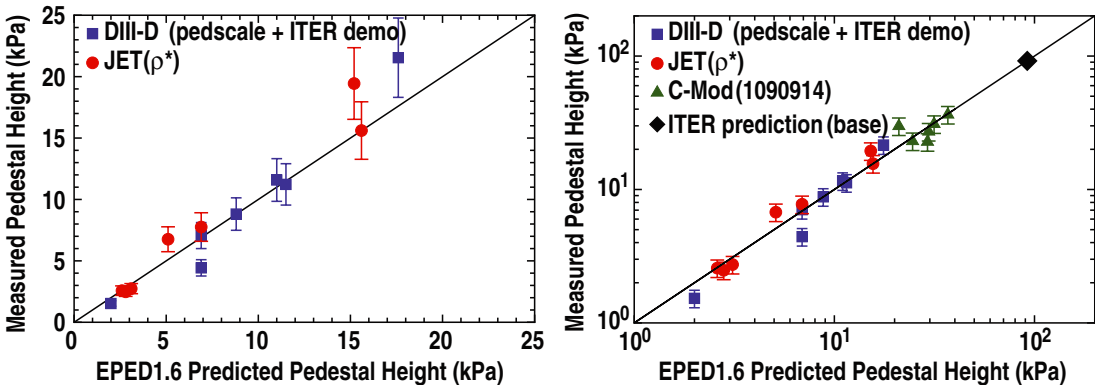

Figure 8. (*a*) Comparison of EPED1.6 predicted pedestal height with measurements on 14 DIII-D and JET discharges. (*b*) Comparison of EPED1.6 predicted pedestal height with measurements on C-Mod, DIII-D, and JET, including prediction for the ITER base case (black diamond), using a log scale. The error bars shown are a simple 15% estimate of the measurement uncertainty, in reasonable agreement with more detailed error analysis [13, 27].

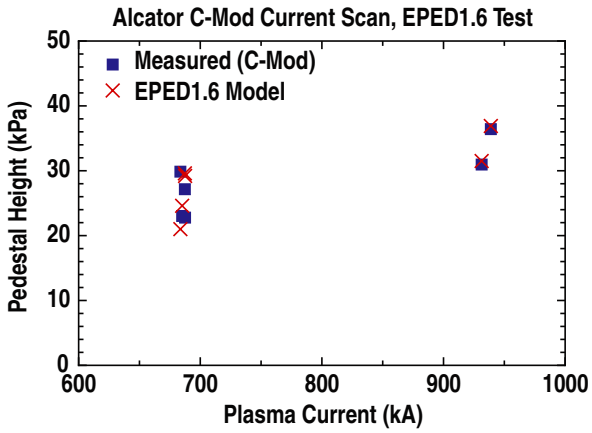

Figure 9. The pedestal height predicted by the EPED1.6 model (X's) is compared with measurements on the Alcator C-Mod tokamak (filled squares) as a function of plasma current.

current discharges have a pedestal electron density $n_{e,ped} \sim (1.12–1.25) \times 10^{20}\,m^{-3}$ and the high current discharges have $n_{e,ped} \sim (1.59–1.71) \times 10^{20}\,m^{-3}$. Note that the magnetic field is similar to the ITER reference value (5.3 T) and that the pedestal density is somewhat higher than that expected for ITER. High resolution Thomson scattering measurements [32] are used to determine the pedestal electron temperature and density, and the pedestal height is taken to be twice the measured electron pressure.

A comparison of the observed pedestal height with the EPED1.6 model is given in figure 9, as a function of plasma current. For these six cases, the ratio of predicted to observed pedestal height is 1.03 ± 0.19. The model correctly predicts the observed trend in pedestal height with current, finding an average 31% increase in pedestal height (from 26.1 to 34.2 kPa), in going from low (~686 kA) to high (~935 kA) current, in good agreement with the observed 31% increase (from 25.7 to 33.7 kPa) in pedestal height in response to the ~36% increase in current.

The results of the comparison of the EPED1.6 model with these new experiments on Alcator C-Mod are plotted alongside the comparisons with JET and DIII-D in figure 8(*b*). For the complete set of 20 studied cases on the three devices, the ratio of predicted to observed pedestal height is 1.02 ± 0.20, with a correlation coefficient of 0.96 between the model and the observations.

5. EPED1.6 predictions for ITER

Combining the DIII-D, JET and C-Mod comparisons (figure 8(*b*)), the EPED1.6 model has been successfully tested over a factor of 23 in pedestal height. Using the model to predict the ITER pedestal height for its baseline parameters, we find an expected pedestal height of $\beta_{N,ped} \sim 0.6$, or $p_{ped} \sim 92$ kPa, less than a factor of 3 above the range studied, as shown by the black diamond in figure 8(*b*). The predicted ITER pedestal width is $\Delta_{\psi_N} \sim 0.04$ (both predictions are similar to those for EPED1, discussed in [5, 12]). The accuracy of these predictions is expected to be ~20% based on the studies in section 4. We note that the predicted pedestal in ITER is in the low collisionality kink/peeling limited regime, where quiescent H-mode operation is possible, and pedestal height increases with density. The predicted height and width depend on the precise values chosen for the inputs $\boldsymbol{I}$, and optimization is possible, both of the pedestal itself, and of the combined pedestal–core system, by combining EPED with global MHD calculations and a core transport model such as TGLF [33].

An initial optimization of the ITER pedestal with respect to pedestal density and global Shafranov shift has been performed using the EPED1.6 model, as illustrated in figure 10. The predicted pedestal height increases with density, as shown by the solid lines in figure 10. This is because the stability of the ITER pedestal is limited by current-driven kink/peeling modes (i.e. the predominantly current-driven branch of P–B), due to its low collisionality and moderately strong shaping. Increasing density increases collisionality at a given pressure, and hence decreases the bootstrap current at a given pressure, resulting in a stability bound that increases with density. The global Shafranov shift is generally stabilizing, as discussed in [9]. In figure 10, two values of the global volume averaged normalized pressure, $\beta_N = 1.7$ (circles) and 2.5 (squares), are shown, corresponding to relatively low and high values of the global Shafranov shift. As expected, larger global Shafranov

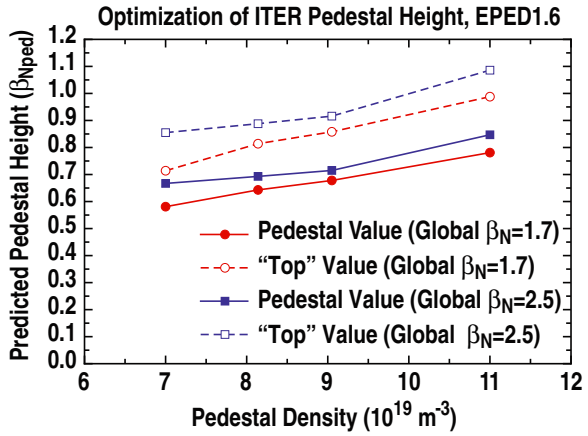

Figure 10. The EPED1.6 predicted pedestal height for the ITER base case is shown as a function of pedestal density for two values of the global normalized pressure. The closed symbols give the pedestal height at a radial location one half-width inside the centre of the edge barrier (i.e. the traditional definition as shown in figure 1(*a*)). The open symbols give the predicted pedestal height at a radial location two half-widths inside the centre of the edge barrier, a location, which is useful for interfacing with core transport models.

shift increases the predicted pedestal height, but the effect is fairly modest.

The solid symbols in figure 10 give the pedestal height at the traditionally defined radial location one half-width (of the tanh) inside the centre of the edge barrier, as defined in [4] and shown for example in figure 1(*a*). For interfacing with core transport codes, it is useful to consider a boundary condition further in, where the profiles are flatter. We define a pedestal 'top' to be two half-widths inside the centre of the edge barrier, a location at which the profile scale lengths have returned to modest values, and a convenient location for an interface between the pedestal model and a core transport model such as TGLF. The 'top' values are shown by dashed lines in figure 10. TGLF calculations find that a 'top' value of $\beta_{\mathrm{Nped}} \sim 0.9$ (approximately independent of density) is needed for high performance operation in ITER [33], a value that EPED1.6 predicts can be reached at sufficient pedestal density, as shown by the dashed lines in figure 10.

6. Discussion and future work

We have developed and successfully tested a model for the pedestal height and width in high-performance H-modes based upon two fundamental and calculable constraints: (1) onset of non-local P–B modes at low to intermediate mode number, (2) onset of nearly local KBMs at high mode number. The present version of the model, EPED1.6, calculates both constraints directly, has no parameters fit to observation, and accurately predicts the pedestal height in a set of 20 DIII-D, JET and C-Mod discharges (ratio of 1.02 ± 0.20 and correlation coefficient of 0.96 between predicted and observed pedestal height).

Predictions are made for the pedestal height and width in ITER, including an initial optimization study of pedestal height as a function of density and global Shafranov shift. Initial indications are that, with proper optimization, ITER should be able to achieve its $Q = 10$ objective, but further study, including additional iteration between core and pedestal models is required to confirm this conclusion. ITER will face the additional challenge of avoiding large ELMs while operating with a high pedestal. Fortunately, the ITER pedestal is predicted to be in the low collisionality kink/peeling limited regime where both ELM-free quiescent H-mode and resonant magnetic perturbation (RMP) ELM suppression have been demonstrated. Further quantitative understanding of these regimes is required to determine under what conditions ITER can meet the other criteria for operation in these regimes.

Development of the EPED model is ongoing, with a fully gyrokinetic version of the BCP technique planned to improve accuracy, especially for low aspect ratio, very strongly shaped discharges. It is also of interest to study possible methods for the separate prediction of density and temperature pedestal widths. Additional dedicated tests on multiple devices are planned.

Acknowledgment

This work was supported in part by the US Department of Energy under DE-FG03-95ER54309, DE-AC05-00OR22725, DE-FG02-92ER54141 and DE-FC02-99ER54512.

References

[1] Connor J.W. *et al* 1998 *Phys. Plasmas* **5** 2687
[2] Snyder P.B. *et al* 2002 *Phys. Plasmas* **9** 2037
[3] Wilson H.R. *et al* 2002 *Phys. Plasmas* **9** 1277
[4] Snyder P.B. *et al* 2004 *Plasma Phys. Control. Fusion* **46** A131
[5] Snyder P.B. *et al* 2009 *Nucl. Fusion* **49** 085035
[6] Huysmans G.T.A. 2005 *Plasma Phys. Control. Fusion* **47** B165
[7] Wilson H.R. *et al* 2006 *Plasma Phys. Control. Fusion* **48** A71
[8] Saarelma S. *et al* 2009 *Plasma Phys. Control. Fusion* **51** 035001
[9] Snyder P.B. *et al* 2007 *Nucl. Fusion* **47** 961
[10] Aiba N. *et al* 2006 *Comput. Phys. Commun.* **175** 269
[11] Aiba N. *et al* 2009 *Nucl. Fusion* **49** 065015
[12] Snyder P.B. *et al* 2009 *Phys. Plasmas* **16** 056118
[13] Groebner R.J. *et al* 2009 *Nucl. Fusion* **49** 085037
[14] Roberts K.V. and Taylor J.B. 1962 *Phys. Rev. Lett.* **8** 197
[15] Tang W.M. *et al* 1982 *Nucl. Fusion* **22** 1079
[16] Dudson B.D. *et al* 2009 *Comput. Phys. Commun.* **180** 1467
[17] Xu X.Q. *et al* 2010 *Phys. Rev. Lett.* **105** 175005
[18] Rewoldt G. *et al* 1987 *Phys. Fluids* **30** 807
[19] Hong B.-G. *et al* 1989 *Phys. Fluids* B **1** 1589
[20] Snyder P.B. 1999 *PhD Thesis* Princeton University
[21] Snyder P.B. and Hammett G.W. 2001 *Phys. Plasmas* **8** 744
[22] Jenko F. and Dorland W. 2001 *Plasma Phys. Control. Fusion* **43** A141
[23] Candy J. 2005 *Phys. Plasmas* **12** 072307
[24] Urano H. *et al* 2008 *Nucl. Fusion* **48** 045008
[25] Beurskens M.N.A. *et al* 2008 *Nucl. Fusion* **48** 095004
[26] Beurskens M.N.A. *et al* 2009 *Plasma Phys. Control. Fusion* **51** 124051
[27] Beurskens M.N.A. *et al* 2011 *Phys. Plasmas* **18** 056120
[28] Doyle E.J. *et al* 2010 *Nucl. Fusion* **50** 075005
[29] Osborne T.H. *et al* 2010 *Proc. 23rd Int. Conf. on Fusion Energy (Daejeon, Korea, 2010)* (Vienna: IAEA) CD-ROM file EXC/2-1 and http://www-naweb.iaea.org/napc/physics/FEC/FEC2010/html/index.htm
[30] Marmar E. *et al* 2009 *Nucl. Fusion* **49** 104014
[31] Terry J. *et al* 2007 *J. Nucl. Materials* **363** 994
[32] Hughes J.W. *et al* 2001 *Rev. Sci. Instrum.* **72** 1107
[33] Kinsey J.E. *et al* 2011 *Nucl. Fusion* **51** 083001